1 **AERONET-based nonspherical dust optical models and effects on the VIIRS Deep**

2 **Blue/SOAR over-water aerosol product**

3

4 **Jaehwa Lee[1,2], N. Christina Hsu[1], Andrew M. Sayer[1,3], Corey Bettenhausen[1,4], and Ping**

5 **Yang[5]**

6

7 [1]NASA Goddard Space Flight Center, Greenbelt, Maryland, USA

8 [2]Earth System Science Interdisciplinary Center (ESSIC), University of Maryland, College Park,

9 Maryland, USA

10 [3]Goddard Earth Science Technology and Research (GESTAR), Universities Space Research

11 Association, Columbia, Maryland, USA

12 [4]ADNET Systems Inc., Bethesda, Maryland, USA

13 [5]Department of Atmospheric Sciences, Texas A&M University, College Station, Texas, USA

14

15 Corresponding author: Jaehwa Lee (jaehwa.lee@nasa.gov)

16

17 **Key Points:**

18 • AERONET-based nonspherical dust optical property model for use in NASA's VIIRS

19 Deep Blue/SOAR over-water algorithm

20 • Significant improvements in SOAR aerosol product over dust layers

21 • Enhanced view of global aerosol properties by VIIRS Deep Blue algorithm suite

22

23

Abstract

Aerosol Robotic Network (AERONET)-based nonspherical dust optical models are developed and applied to the Satellite Ocean Aerosol Retrieval (SOAR) algorithm as part of the Version 1 Visible Infrared Imaging Radiometer Suite (VIIRS) NASA 'Deep Blue' aerosol data product suite. The optical models are created using Version 2 AERONET inversion data at six distinct sites influenced frequently by dust aerosols from different source regions. The same spheroid shape distribution as used in the AERONET inversion algorithm is assumed to account for the nonspherical characteristics of mineral dust, which ensures the consistency between the bulk scattering properties of the developed optical models with the AERONET-retrieved microphysical and optical properties. For the Version 1 SOAR aerosol product, the dust optical models representative for Capo Verde site are used, considering the strong influence of Saharan dust over the global ocean in terms of amount and spatial coverage. Comparisons of the VIIRS-retrieved aerosol optical properties against AERONET direct-Sun observations at three island/coastal sites suggest that the use of nonspherical dust optical models significantly improves the retrievals of aerosol optical depth (AOD) and Ångström exponent by mitigating the well-known artifact of scattering angle dependence of the variables observed when incorrectly assuming spherical dust. The resulting removal of these artifacts results in a more natural spatial pattern of AOD along the transport path of Saharan dust to the Atlantic Ocean; i.e., AOD decreases with increasing distance transported, whereas the spherical assumption leads to a strong wave pattern due to the spurious scattering angle dependence of AOD.

1 Introduction

Mineral dust, among other aerosol types, is one of the key constituents in the terrestrial atmosphere, producing important climate forcing through directly perturbing radiation balance [*Liao and Seinfeld*, 1998; *Li et al.*, 2004; *Lee et al.*, 2014] and interacting with clouds [*Yin et al.*, 2002; *Yoshioka et al.*, 2007; *Cziczo et al.*, 2013]. It contributes to a significant portion of the global aerosol loadings thereby responsible for a large amount of the aerosol radiative effect [*Tegen et al.*, 1997; *Chin et al.*, 2014].

One of the important characteristics of mineral dust particles from light scattering perspective are their nonspherical geometric shape, which makes the Lorenz-Mie theory inappropriate for the calculation of their scattering properties. To overcome this issue, numerous efforts have been made to accurately compute the light scattering of nonspherical particles, including the T-matrix method [*Waterman*, 1971; *Mishchenko and Travis*, 1994], the discrete dipole approximation [*Draine and Flatau*, 1994; *Yurkin et al.*, 2007], the finite-difference time domain method [*Yee*, 1966; *Yang and Liou*, 1995, 1996; *Yang et al.*, 2000], and geometric optics method [*Yang et al.*, 2007; *Bi et al.*, 2009]. Each methodology has different advantages and disadvantages in terms of computational time, and applicable particle morphology and size regimes.

Although spheroid mixtures [e.g. *Mishchenko et al.*, 1997] are not representative for 'real' dust in terms of geometric shape, they mimic the scattering and absorption characteristics of realistic dust particles reasonably well if appropriate refractive indices and shape distribution are used [*Dubovik et al.*, 2006; *Kemppinen et al.*, 2015]. Consequently, spheroid mixtures have been used in aerosol inversion algorithms for ground-based and spaceborne instruments given the fact that it is impractical to implement ever-changing dust morphologies in the algorithms [*Kahn et al.*, 1997; *Dubovik et al.*, 2006; *Feng et al.*, 2009; *Lee et al.*, 2012].

Since aerosols are ubiquitous and show complex spatiotemporal distributions over the globe, satellite observations have been recognized as an important source of data, with the ability to observe extensive areas at a high spatiotemporal resolution [*Kaufman et al.*, 2002]. Satellite algorithms to retrieve aerosol optical properties using visible to shortwave infrared bands generally incorporate lookup tables of calculated TOA (top of the atmosphere) reflectance for various aerosol types (or aerosol optical models) to compare the simulated TOA reflectance against the measurements made by the satellite sensors in their retrieval implementations.

76 Therefore, the simulation of the TOA reflectance needs to be highly accurate, and thus demands
77 realistic aerosol optical property models in the radiative transfer calculations.

78 As one of the NASA's operational aerosol retrieval algorithms, the Deep Blue aerosol
79 project (https://deepblue.gsfc.nasa.gov) has provided long-term global aerosol data records over
80 both land and water surfaces using Sea-viewing Wide Field-of-view Sensor (SeaWiFS) from
81 1997 to 2010 [*Hsu et al.*, 2004, 2006, 2013; *Sayer et al.*, 2012a, 2012b] and over land using the
82 twin Moderate Resolution Imaging Spectroradiometer (MODIS) sensors aboard Terra from 2000
83 onwards and Aqua from 2002 onwards [*Hsu et al.*, 2013; *Sayer et al.*, 2013, 2014, 2015]. The
84 Deep Blue algorithm is renowned for its application to bright land surfaces such as desert, which
85 is accomplished by the use of blue bands (412 and 470 nm for MODIS or 490 nm for SeaWiFS)
86 in the retrieval process. With the launch of the Suomi National Polar-orbiting Partnership (S-
87 NPP) satellite in late 2011, the algorithm now extends its application to the measurements made
88 by the Visible Infrared Imaging Radiometer Suite (VIIRS) instrument to continue the Deep Blue
89 aerosol data record beyond the Earth Observing System era. Like SeaWiFS, the VIIRS Deep
90 Blue will produce data over both land and water surfaces as retrieved by the enhanced Deep Blue
91 [*Hsu et al.*, 2013] and Satellite Ocean Aerosol Retrieval (SOAR) algorithms [*Sayer et al.*, 2017],
92 respectively.

93 The Deep Blue algorithm applied to land surfaces includes a nonspherical dust optical
94 model with an empirical phase function that well matches the AERONET-derived dust phase
95 function in backscattering direction [*Hsu et al.*, 2004]. However, the prior application of SOAR
96 only incorporated spherical dust, which resulted in biases in aerosol properties over regions
97 where dust aerosols are frequently observed. It is well known that the spherical assumption leads
98 to an unrealistic scattering angle dependence of aerosol optical depth (AOD) (as well as
99 Ångström exponent) mainly due to poor representation of the shape of the phase function
100 [*Masuda et al.*, 2002; *Levy et al.*, 2003; *Mishchenko et al.*, 2003; *Wang et al.*, 2003; *Lee et al.*,
101 2012; *Banks et al.*, 2016]; i.e., it results in an overestimation in the side-scattering direction (80°
102 $< \Theta < 150°$) and an underestimation in the backscattering direction ($\Theta > 150°$) with a bias as
103 high as 50%.

104 The foci of the present study are to develop nonspherical dust optical models for SOAR,
105 to analyze the effects of the new optical models on the aerosol retrieval performance, and to
106 provide a further practical illustration of the type of artifacts which can arise from the

107 assumption of spherical dust in satellite remote sensing algorithms. Although the results are

108 illustrated for the application to SOAR and VIIRS data, these optical models are more broadly

109 applicable to any aerosol property retrieval. Section 2 summarizes the data and methodology

110 used, and section 3 addresses dust optical models developed for SOAR. In section 4, the effects

111 of the nonspherical dust optical model on retrieval performance are discussed. Finally, the major

112 findings of this study are summarized in section 5.

113

114 **2 Data and Methods**

115 2.1 AERONET direct-Sun and inversion data

116   Aerosol Robotic Network [AERONET, *Holben et al.*, 1998] direct-Sun and inversion

117 products are used to develop dust optical models for use in the SOAR algorithm and validate the

118 SOAR-retrieved aerosol products. We only consider cloud-screened and quality-assured Level 2

119 products to minimize potential errors due to cloud contamination and other error sources

120 [*Dubovik et al.*, 2000; *Smirnov et al.*, 2000; *Holben et al.*, 2006]. The main purpose of the direct-

121 Sun measurements is to provide spectral AOD (τ_λ; where λ is wavelength) at multiple

122 wavelengths ranging from 340 to 1640 nm. The wavelength range and number of channels

123 within the range vary with the sites (440, 675, 870, and 1020 nm being standard). Data are

124 provided at a temporal resolution of ~5 – 15 min with an AOD uncertainty of 0.01 – 0.02

125 [*Holben et al.*, 1998; *Eck et al.*, 1999]. Ångström exponent (hereafter denoted as AE or α), a

126 qualitative indicator of aerosol particle size [*Ångström*, 1929], can be derived as the slope of

127 spectral AOD across a certain wavelength range on a logarithmic scale,

128     $\alpha = -\frac{\ln(\tau_{\lambda 1}) - \ln(\tau_{\lambda 2})}{\ln(\lambda 1) - \ln(\lambda 2)}.$ (1)

129 In this investigation AERONET α is defined across the spectral range 440 – 870 nm.

130   The AERONET inversion algorithm [*Dubovik and King*, 2000; *Dubovik et al.*, 2006]

131 makes use of sky radiance observations in the solar almucantar in combination with direct-Sun

132 data to retrieve the microphysical and optical properties of aerosols, which are required to

133 calculate their bulk scattering properties (as opposed to single-scattering properties for individual

134 particles). The bulk scattering properties include spectral AOD, the single-scattering albedo

135 (SSA), and the phase function (or the phase matrix for vector radiative transfer model), which

136 are the key parameters needed for radiative transfer calculations. The inversion data include

137 aerosol size distribution, spectral complex refractive indices at four wavelengths, and percentage

138 of scattering arising from spherical particles (also known as "sphericity parameter"), retrieved as

139 best matching the observed sky radiances in a wide scattering angle range ($2° − 2 ×$ solar zenith

140 angle), given spectral AOD observed by the direct-Sun measurement.

141 The size distribution is binned at 22 logarithmically-spaced radii ranging from $0.05 − 15$

142 μm. Then, the size distribution parameters, including volume concentration (C_v), volume median

143 radius (r_v), geometric standard deviation (σ), and effective radius (r_{eff}), can be derived from the

144 retrieved size distribution. Although AERONET does not impose a distribution shape, these

145 parameters are often used to define a bimodal lognormal volume size distribution,

146
$$\frac{dV(r)}{d\ln r} = \sum_{i=1}^{2} \frac{C_{v,i}}{\sqrt{2\pi}\sigma_i} e^{-\frac{1}{2}\left(\frac{\ln r - \ln r_{v,i}}{\sigma_i}\right)^2}. \tag{2}$$

147 Note that in the AERONET inversion, the fine and coarse modes are separated at the inflection

148 point within the size interval $0.439 − 0.992$ μm, and the size distribution parameters are provided

149 for each mode. The effective radius is defined as the ratio of the third to second moments of the

150 number size distribution, which represents mean particle radius weighted by projected area, as

151 first introduced by Hansen and Travis (1974) in the form,

152
$$r_{eff} = \frac{\int_{r_{min}}^{r_{max}} r^3 \frac{dN(r)}{d\ln r} d\ln r}{\int_{r_{min}}^{r_{max}} r^2 \frac{dN(r)}{d\ln r} d\ln r}. \tag{3}$$

153 Although the size distribution and effective radius of nonspherical particles can be represented

154 by more generalized forms, Eqs. (2) and (3) are used in the AERONET inversion, as it assumes

155 volume-equivalent spheres for nonspherical particles [*Dubovik et al.*, 2006].

156 Both the real and imaginary parts of the refractive index are provided at the four

157 wavelengths (440, 675, 870, and 1020 nm), assuming a single refractive index representative for

158 the whole size distribution range. Note that, while this may cause issues in the case where both

159 fine and coarse modes of different compositions contribute significantly to the total AOD, but in

160 the case of dust aerosols the coarse mode is typically optically dominant and the aforementioned

161 issue is much less concerned. The wavelength- and size mode-independent sphericity parameter

162 (100% − nonsphericity parameter) describes the degree of aerosol nonsphericity, as it represents

163 the relative contributions of spherical and nonspherical particles to the final bulk scattering

164 properties, given microphysical and optical properties retrieved. A fixed spheroid shape

165 distribution is assumed for the nonspherical component (see Fig. 13 in *Dubovik et al.*, 2006).

166

2.2 Aerosol single-scattering property database

Since AERONET inversions only provide aerosol bulk scattering properties at selected wavelengths (and also do not provide the full phase matrix), they must be extended to VIIRS wavelengths to create the lookup tables for the SOAR algorithm. To this end, we incorporate a single-scattering property database for individual ellipsoidal particles (including spherical and spheroidal particles) developed by *Meng et al.* [2010]. This saves tremendous computational time that is required for calculating the single-scattering properties of spheroids for wide ranges of particle sizes and aspect ratios. The databases were created by employing four different computational methods for different particle size parameter and shape regimes: Mie theory [*Bohren and Huffman*, 1983] for spherical particles, T-matrix method [*Mishchenko et al.*, 1997] and discrete dipole approximation [*Yurkin et al.*, 2007] for spheroidal and ellipsoidal particles with small-to-moderate size parameters (up to $20 - 40$), respectively, and an improved geometric optics method [*Yang et al.*, 2007; *Bi et al.*, 2009] for ellipsoidal particles (including spheroids) with large size parameters (higher than $10 - 20$).

The database takes in inputs that cover wide ranges of size parameters ($0.025 - 1000$), refractive index ($1.1 - 2.1$ for the real part and $0.0005 - 0.5$ for the imaginary part), and two aspect ratios ($0.3 - 1$ describing deformation of spheres in both semi-major and semi-minor axes), which are useful for various applications and cover the range of values expected for terrestrial aerosol remote sensing/modeling [e.g. *Lee et al.*, 2012; *Colarco et al.*, 2014; *Buchard et al.*, 2015; *Kemppinen et al.*, 2015]. A software package is also included in the database to provide interpolated results in the case that the microphysical and optical parameters are provided between the database node points, and to generate bulk scattering properties integrated over certain particle size and shape distributions. Among other outputs, we use the phase matrix, and extinction and scattering efficiencies of individual particles to create bulk scattering properties for dust size distributions that will be derived later in this work, given the AERONET's spheroid shape distribution.

Figure 1 shows an example of bulk scattering properties (AOD, SSA, and phase function) from AERONET superimposed with those from the database assuming spherical particles and sphere/spheroid mixtures as a function of the sphericity parameter (hereafter, "sphere/spheroid mixture" will be referred to as simply "spheroid" for brevity). A severe dust event observed at

197 Capo Verde with the sphericity parameter of 0.69% was chosen. It is found that the database
198 accurately produces the AERONET-retrieved spectral AOD (generally within 1%), SSA (within
199 3% or better depending on wavelength), and the phase function (within 0.05 for scattering angles
200 > 30°; note VIIRS and most other spaceborne sensors generally observe scattering angles in the
201 range ~80°-180°). The spherical assumption results in larger differences than the spheroid case,
202 particularly in the phase function, demonstrating possible scattering angle-dependent errors in
203 the satellite-retrieved aerosol optical properties for dust-laden cases. The slight differences
204 observed for the spheroid case are likely due to the difference in handling the size distribution
205 when integrating the single-scattering properties (trapezoidal approximation for AERONET
206 inversion [*Dubovik et al.*, 2006] vs. linear interpolation in this study). The difference in the
207 single-scattering property databases used, i.e., different node points for size parameter, refractive
208 index, and aspect ratio between AERONET inversion and this study, can also cause slightly
209 differences in the final bulk scattering properties due to the errors caused by interpolations
210 between the node points.

211
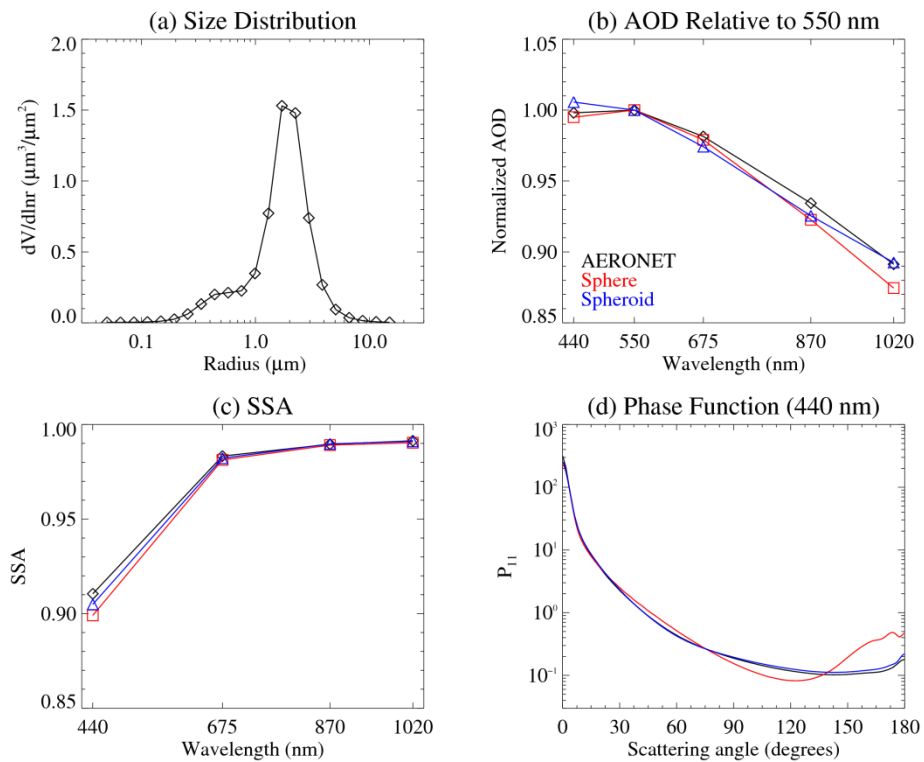
212

213 Figure 1. (a) AERONET size distribution, (b) spectral AOD relative to 550 nm, (c) spectral SSA,
214 and (d) phase function at 440 nm for a dust case observed at Capo Verde at 10:24 a.m. UTC, 9

215 March 2006. Aerosol optical properties derived from the single-scattering property database are
216 superimposed in (b-d) for spherical (red) and spheroidal (blue) models.

217

218 2.3 SOAR algorithm for VIIRS

219 Here we provide a brief description of the VIIRS SOAR algorithm and its data products.
220 The initial application to SeaWiFS was described fully by *Sayer et al.* [2012b]; information on
221 the VIIRS application can be found in *Sayer et al.* [2017], and a full description of the VIIRS
222 application will be provided in a follow-up study.. SOAR provides aerosol optical properties
223 including AOD and fine-mode AOD fraction (FMF) at 550 nm, 440-870 nm AE, aerosol type
224 (marine, fine-dominated, or dust), and spectral AOD (at 488, 555, 672, 865, 1240, 1610, and
225 2250 nm). The data products are provided at a nominal spatial resolution of 6 km $\times$ 6 km (8×8
226 pixel aggregation) at the sub-satellite point over cloud- and snow/ice-free water surfaces. The
227 inversion procedure to convert the TOA reflectances measured by VIIRS into aerosol optical
228 properties incorporates lookup tables calculated for three aerosol optical models for different
229 AOD and FMF (both at 550 nm) regimes: marine model for AOD range $0.001 - 0.25$ and FMF
230 range $0.0 - 0.9$, fine-dominated model for AOD range $0.15 - 5.0$ and FMF range $0.7 - 1.0$, and
231 dust model for AOD range $0.15 - 5.0$ and FMF range $0.0 - 0.6$. The minimization procedure
232 tests the χ^2 statistic between observed and calculated TOA reflectances to simultaneously
233 retrieve AOD and FMF and to find best aerosol optical model out of the three. No mixing
234 between the optical models is assumed.

235 The dust optical model is developed in a way to minimize changes in the algorithm (and
236 lookup table) structure of SOAR (i.e., separated from other optical models as no combination
237 between models are assumed). In addition, it has flexibility to include different fine-mode
238 component when necessary. *Sayer et al.* [2014] suggested that biomass burning smoke aerosols
239 from different sources and burning types can show significantly different optical properties from
240 one another and also from the fine-dominated optical model assumed in the SOAR algorithm.
241 This has implications that AOD biases over certain regions can be due to this variety of optical
242 properties and thus can be reduced if more appropriate aerosol models are used. For future
243 implementation of this variety, bulk scattering properties of fine- and coarse-mode are created
244 separately under the assumption of bimodal lognormal size distribution, and are combined as a
245 function of FMF for the bulk scattering properties. This facilitates future creation of dust optical

246 models mixed with various fine-mode aerosols, such as urban pollution and biomass burning
247 smoke from various sources. In addition, when creating optical models with intermediate FMF,
248 we can avoid using the inversion data for fine/coarse mixed conditions, for which the inversion
249 data are thought to be less accurate due to the assumption of homogeneous particles (i.e., a single
250 refractive index for particles of all sizes) [*Dubovik and King*, 2000].

251

252 **3 Creating Dust Optical Models for SOAR**

253 We derive the microphysical and optical properties of coarse-mode dust from different
254 source regions based on AERONET inversion data. The properties are then used for obtaining
255 bulk scattering properties through the single-scattering property database, which will eventually
256 be used in creating the dust lookup table for SOAR.

257

258 3.1 Microphysical and optical properties of dust as seen by AERONET

259 To analyze microphysical and optical properties of dust-dominated aerosols, global
260 AERONET inversion data are filtered first for FMF (550 nm) < 0.2, coarse-mode AOD (550 nm)
261 > 0.5, and sphericity parameter < 1%. The choice of these thresholds is to minimize the effects of
262 fine-mode aerosols that are chemically different from dust (small FMF), the uncertainty in the
263 inversion algorithm (high AOD), and non-dust coarse-mode aerosols (low sphericity) on the
264 inversion products for dust properties while maintaining sufficient number of data points [cf.
265 *Dubovik et al.*, 2000; *Lee et al.*, 2012; *Schuster et al.*, 2016]. Although these thresholds are
266 somewhat subjective, variations within a reasonable range only negligibly affect the resulting
267 models. Then, medians are used to represent the dust aerosols observed at each AERONET site,
268 to reduce the sensitivity to anomalous conditions or AERONET retrieval errors.

269 Figure 2 shows a large-scale view of dust microphysical and optical properties at
270 locations where dust aerosols, defined by the above filters, are frequently observed (number of
271 data points > 30). The median coarse-mode effective radius suggests larger particle sizes over
272 India and China than over North Africa and the Arabian Peninsula, possibly due to differences in
273 transport distance and wind speed [*Kok*, 2011]. It is worthwhile to note that a decreasing
274 tendency of particle size of dust generated in the Bodélé Depression (decreasing effective radius
275 from east to west over North Africa) is detected during the transport likely due to faster dry
276 deposition of larger particles [*Giorgi*, 1986; *Lin et al.*, 1994]. In addition, the smaller effective

radii in the coastal regions imply that using data from inland AERONET sites for ocean algorithm could lead to an overestimation of particle size, which can in turn result in an overestimation in the satellite-retrieved AOD due to an underestimation in the aerosol backscattering fraction (the larger the particle size, the lower the backscattering fraction).
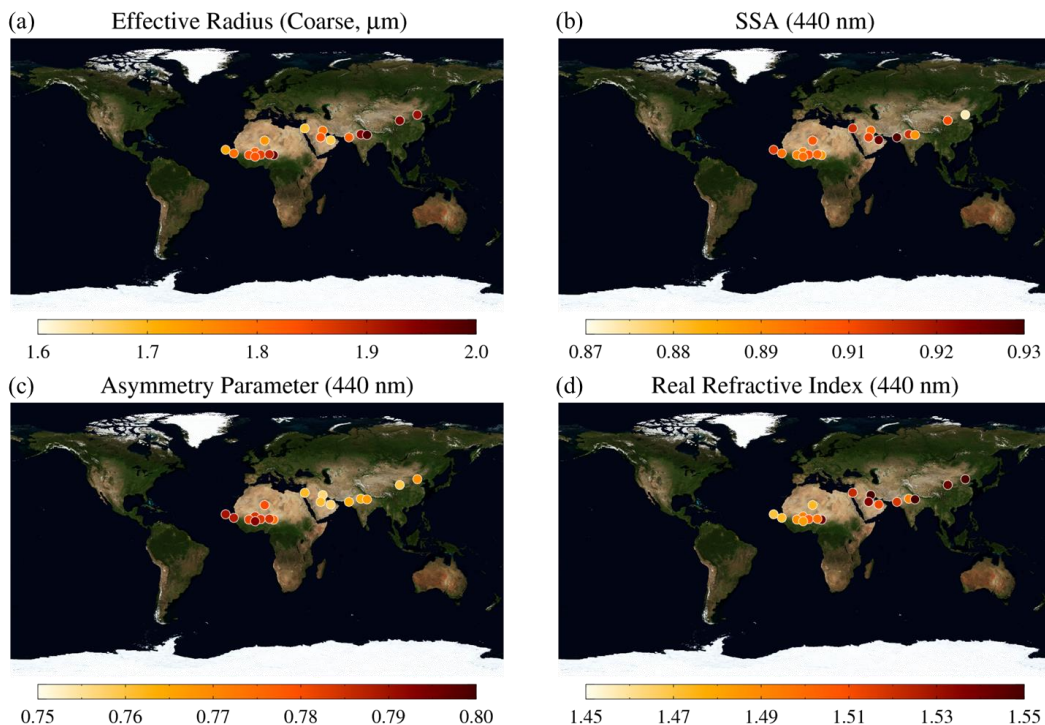
Figure 2. Median (a) effective radius (coarse-mode), (b) SSA, (c) asymmetry parameter, and (d) the real part of the refractive index of dust-dominated aerosols derived from AERONET inversion data over various locations. Values in (b-d) are for 440 nm. Sites are shown only if the number of data points that meet the requirement for dust-dominated case (discussed in the text) is higher than 30.

The SSA at 440 nm, where strong absorption by mineral dust occurs, generally ranges from 0.87 to 0.93, showing a minimum of ~0.875 at Xianghe, China. The low SSA at Xianghe is mainly due to the effect of the reddish (as opposed to whitish) dust (strong absorption in blue wavelength) from Inner Mongolia as well as possible internal mixing with carbonaceous aerosols [*Scarnato et al.*, 2015; *Sugimoto et al.*, 2015]. The maxima of ~0.925 at Mezaira, Abu Dhabi and Karachi, Pakistan are associated with the relatively bright (whitish) dust from southeastern Arabian Desert [e.g. *Eck et al.*, 2008] and both transported Arabian dust and dust from local

296 sources in Pakistan and Afghanistan [e.g. *Alam et al.*, 2011], respectively. Aside from the two
297 extremes, 440 nm SSA are generally within the range of 0.89−0.91, suggesting that 440nm SSA
298 of 0.90 can be a reasonable first guess for satellite algorithms.

299 The asymmetry parameter g (cosine-weighted mean of phase function) by definition
300 represents the degree of deviation of scattering from the forward direction, varying from -1 (pure
301 backward scattering) to 1 (pure forward scattering). It is one of the factors determining direct
302 radiative effects of aerosols. From light scattering theory, g depends on particle size (larger
303 particle corresponds to higher g) and refractive index (higher real/imaginary part of the refractive
304 index correspond to lower/higher g, respectively). It shows higher values in North Africa than
305 Asia, demonstrating the real part of the refractive index being stronger than effective radius at
306 controlling the g, which is likely due to the small differences in the effective radii between the
307 sites. Although the complex refractive index is determined by chemical composition of mineral
308 dust, geometric shapes can also be a factor that changes the apparent refractive index, as the
309 AERONET inversion assumes a fixed spheroid shape distribution in the retrieval process [cf.
310 *Kemppinen et al.*, 2015].

311 Figure 3 shows the microphysical and optical properties of dust at six distinct locations
312 (Capo Verde, Solar Village, Mezaira, Kanpur, SACOL; Semi-Arid Climate Observatory, and
313 Xianghe), for which dust optical models are created. The locations are selected to represent dust
314 from different source regions; i.e., Saharan dust for Capo Verde, Arabian dust from different
315 regions for Solar Village and Mezaira, dust from Thar Desert for Kanpur, from Taklimakan and
316 Gobi Desert for SACOL, and from Taklimakan, Gobi, and Inner Mongolia for Xianghe. It is
317 revealed that despite the different sources, some of the properties are similar between different
318 locations, such as the binned volume size distributions peaking at 2.24 μm (with some
319 differences in geometric standard deviations) and rather flat spectral AOD due to coarse-mode
320 optical dominance. However, the 440 nm SSA (and corresponding imaginary part of the
321 refractive index), asymmetry parameter, and the real part of the refractive index denote different
322 optical characteristics of dust from different source regions. The range of SSA for different sites
323 decreases with wavelength, and is only ~0.01 at 870 and 1020 nm. This indicates possible use of
324 a simple SSA assumption for the longer wavelengths. The asymmetry parameter generally
325 decreases with wavelength and flattens for wavelength > 675 nm, still showing strong forward
326 scattering even at the longer wavelengths ($g > 0.7$). The real part of the refractive index generally

327 decreases with wavelength in a magnitude of ~0.04, and the imaginary part, which is highly
328 related to SSA, shows a wide range (0.0027 – 0.0044) at 440 nm and lower values with narrower
329 ranges (0.0007−0.0012) at the longer wavelengths.

330
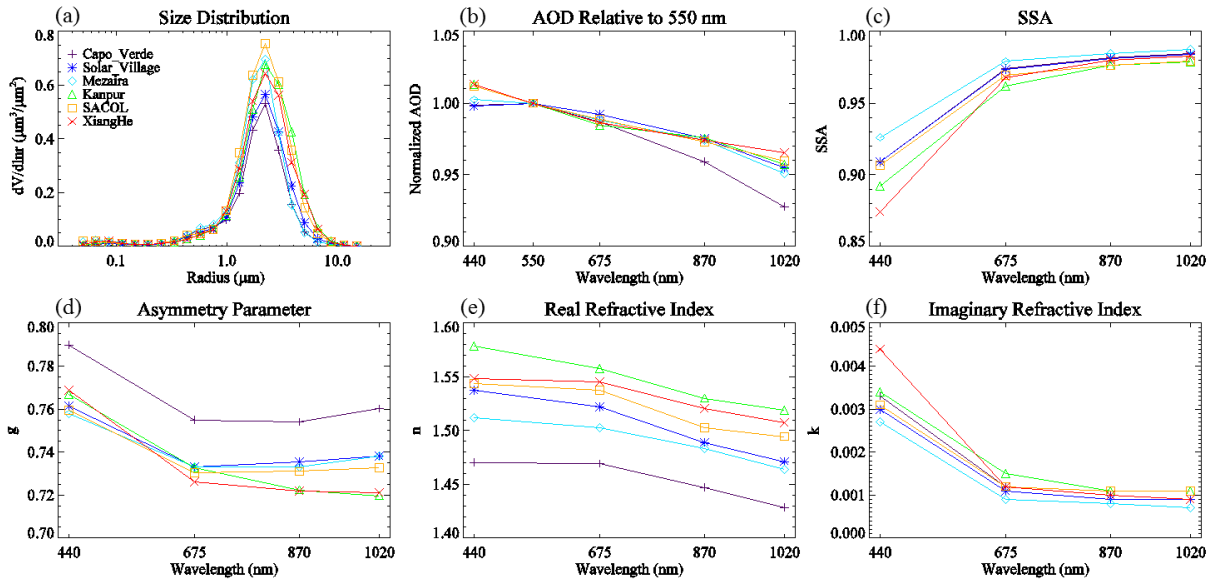
331

332 Figure 3. AERONET-derived median (a) size distribution, (b) spectral AOD relative to 550 nm,
333 (c) SSA, (d) asymmetry parameter, and (e) real and (f) the imaginary part of the refractive index
334 for dust-dominated aerosols at six locations influenced by different source regions.

335

336   We assume that the refractive index of the dust-dominated cases represents coarse-mode
337 dust properties (i.e. the small contribution from the fine-mode for these cases does not
338 significantly affect the average retrieved refractive index). For size distribution, we use
339 AERONET-derived size distribution parameters for coarse-mode (volume median radii and
340 geometric standard deviations) rather than the median size distributions itself, as we intend to
341 create coarse-mode only dust optical models, and the small volume concentrations of the fine-
342 modes (Figure 3a) can make the inflection point separating fine- and coarse-modes ambiguous
343 for the dust-dominated cases. For fine-mode, the same fine-mode optical model used in SOAR
344 for fine-dominated model [*Sayer et al.*, 2012b] is adopted but with reduced imaginary part of the
345 refractive index (from 0.0075 to 0.001). This is to account for the lower imaginary part of the
346 refractive index derived from AERONET for dust-dominated cases (0.0027-0.0044 for 440 nm

347 and 0.0007-0.0014 for $\lambda \geq 675$ nm). Tables 1 and 2 summarize the microphysical and optical

348 properties of coarse-mode dust at the six locations and those of fine-mode, respectively.

349

350 Table 1. Median volume median radius (r_v), geometric standard deviation (σ), and real (n) and

351 imaginary (k) part of the refractive index of coarse-mode dust optical models at six AERONET

352 sites.

Site name	r_v [μm]	σ [μm]	Refractive index (n+ik)			
			440 nm	675 nm	870 nm	1020 nm
Capo Verde	2.00	0.51	1.47+0.0033i	1.47+0.0012i	1.45+0.0010i	1.43+0.0009i
Solar Village	2.10	0.51	1.54+0.0030i	1.52+0.0011i	1.49+0.0009i	1.47+0.0009i
Mezaira	1.91	0.48	1.51+0.0027i	1.50+0.0009i	1.48+0.0008i	1.46+0.0007i
Kanpur	2.36	0.51	1.58+0.0034i	1.56+0.0015i	1.53+0.0011i	1.52+0.0011i
SACOL	2.20	0.50	1.54+0.0031i	1.54+0.0012i	1.50+0.0011i	1.49+0.0011i
Xianghe	2.23	0.52	1.55+0.0044i	1.55+0.0012i	1.52+0.0010i	1.51+0.0009i

353

354 Table 2. Same as Table 1, but for the fine-mode optical model.

Aerosol model	r_v [μm]	σ [μm]	Refractive index (n+ik)			
			440 nm	675 nm	870 nm	1020 nm
weakly absorbing	0.19	0.44	1.43+0.001i	1.43+0.001i	1.43+0.001i	1.43+0.001i

355

356 3.2 Bulk scattering properties of dust optical model

357   Given the size distribution parameters and complex refractive index in Tables 1 and 2, we

358 derive bulk scattering properties by integrating the single-scattering properties of individual

359 particles over the size distribution for fine-mode (spheres) and both size distribution and aspect

360 ratio for coarse-mode (spheroids). As mentioned previously, we assume the same spheroid shape

361 distribution as used in the AERONET inversion algorithm for the coarse-mode (dust), such that

362 the optical model can be consistent with the sky radiance measurements made by AERONET.

363 The fine- and coarse-mode optical models are created separately and then mixed together in the

364 radiative transfer model (VLIDORT; *Spurr*, 2006) for calculating the lookup table for the various

365 FMF values (0.0 – 0.6 with an increment of 0.1). The integration is performed for

366 logarithmically distributed node points; 1000 size parameter nodes between 0.03 and 999 for the

367 fine-mode; 100 size parameter nodes between 0.03 and 999 and 9 reciprocal aspect ratio nodes

368   between 0.3349 and 0.6944 for prolate and oblate particles for the coarse-mode. This integration

369   node density is sufficient to avoid artificial oscillations in the calculated phase matrix elements

370   resulting from lack of convergence. Then, spectral extinction coefficient, SSA, and phase matrix

371   are used for the radiative transfer calculations. For SOAR Version 1 data processing, we assume

372   dust properties representative for Capo Verde site for the coarse-mode, considering the

373   significant contribution of the Saharan dust over the global ocean in terms of amount and spatial

374   coverage. Future versions of the SOAR/Deep Blue product may consider additional dust optical

375   models.

376   Figure 4 shows medians and central 68% intervals of the bulk scattering properties

377   (spectral AOD relative to 550 nm, SSA, and asymmetry parameter representative of the phase

378   function) of the dust optical model together with those derived from AERONET inversion data at

379   the six locations, for various FMF ranges. The bulk scattering properties of the optical model are

380   calculated by combining the values of the fine- and coarse-mode according to FMF of the

381   individual inversions from all of the AERONET sites used. The comparisons suggest that the

382   dust model represents the dust properties from various source regions well, generally showing

383   intermediate values, although it is based only on Capo Verde input data (Figure 4a-4c). This is

384   likely due to the use of the separate fine-mode optical model of which microphysical and optical

385   properties are different from those of Capo Verde and partly due to the fixed size distribution

386   used. The uncertainty in FMF in the inversion data arising from the determination of the

387   inflection point in the retrieved size distribution [cf. *O'Neill et al.*, 2003] can also affect the

388   spectral features, but it does not seem to be a significant factor here. The dust model, as expected,

389   has weaknesses in reproducing optical properties, particularly SSA, for the higher FMF regime

390   (Figure 4k) due to increased influences of fine-mode aerosols with various optical properties

391   depending on locations [e.g. *Dubovik et al.*, 2002], as well as decreased performance of

392   AERONET inversion data for fine/coarse mixed conditions. This discrepancy can be reduced by

393   including more absorbing fine-mode model such as the one used in the SOAR for fine-dominated

394   aerosols [*Sayer et al.*, 2012b] or even more absorbing ones suggested by *Sayer et al.* [2014]. This

395   will be a subject of future study once error characteristics of VIIRS SOAR product have been

396   examined through a long-term global evaluation of the data set. It should be noted that FMF of

397   dust is typically lower than 0.4 (although severe anthropogenic aerosol event mixed with dust

398   can increase the value) [cf. *Dubovik et al.*, 2002; *Eck et al.*, 2010], and fine-dominated model

399   instead of dust is used for FMF > 0.6, such that the impact of using the weakly absorbing fine-

400   mode for the dust optical model can be insignificant.

401
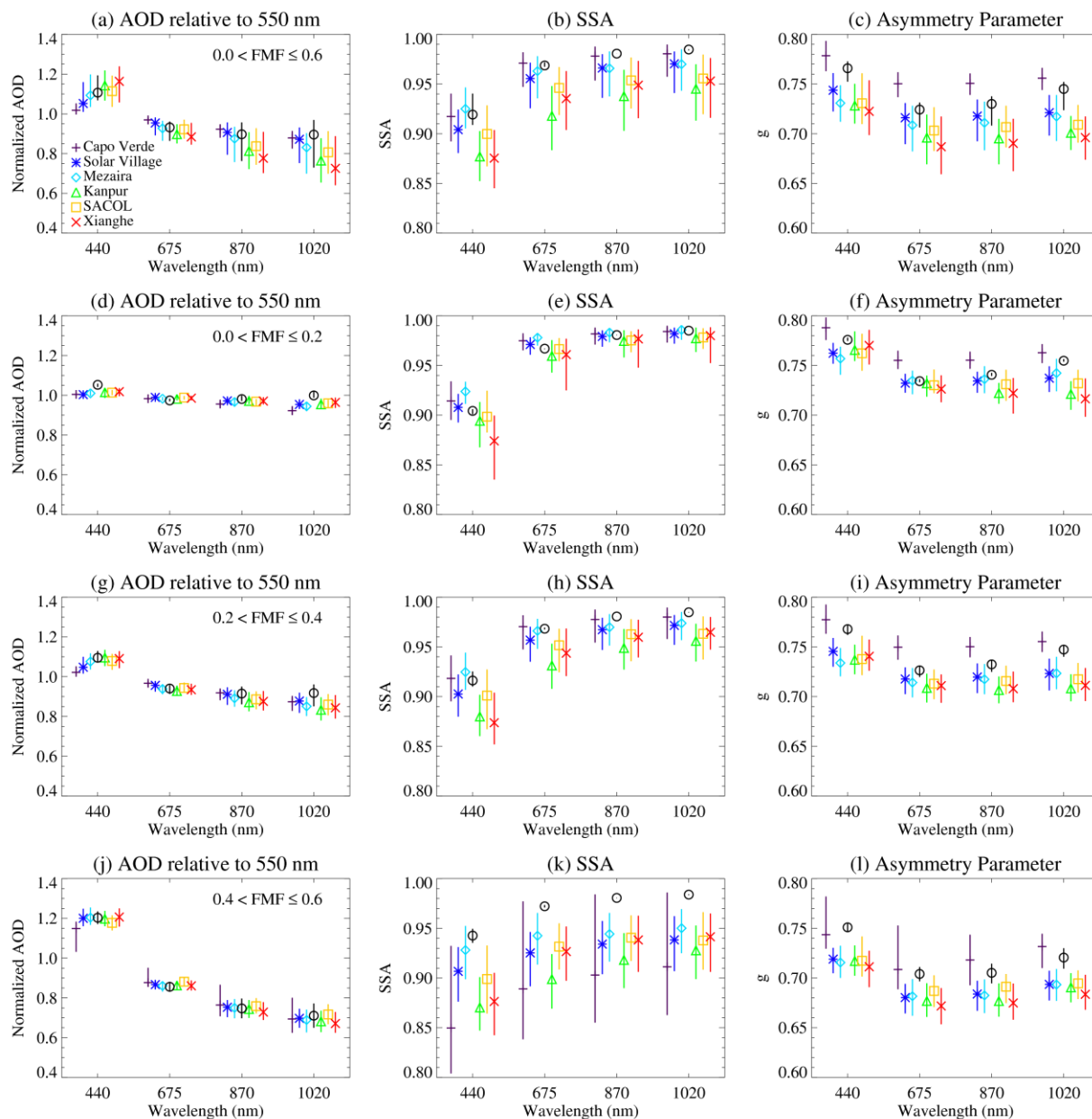
402

403   Figure 4. AERONET (colored symbols) and dust optical model derived (black symbol) spectral

404   AOD relative to 550 nm (left), SSA (middle), and asymmetry parameter (right) for different

405   FMF ranges: (a-c) 0.0 < FMF ≤ 0.6, (d-f) 0.0 < FMF ≤ 0.2, (g-i) 0.2 < FMF ≤ 0.4, and (j-l) 0.4 <

406   FMF ≤ 0.6. AERONET data are for Capo Verde (purple), Solar Village (blue), Mezaira (cyan),

407   Kanpur (green), SACOL (yellow), and Xianghe (red) sites. Note that the colored symbols are

408 purposely offset along the x-axis for a clear illustration, and do not imply actual differences in

409 wavelength. Median and central 68% interval are shown.

410

411 3.3 Extension to VIIRS wavelengths and fine-tuning for optimal performance

412   Since the complex refractive indices from AERONET inversion are limited to

413 wavelength range 440 – 1020 nm, they must be somehow extended to the relevant VIIRS bands

414 (seven bands centered at 488, 555, 672, 865, 1240, 1610, and 2250 nm). The extension for the

415 fine-mode can be done relatively easily because (1) we assume fixed refractive index within the

416 AERONET wavelength range (thus the same real and imaginary values can be used for the

417 VIIRS bands within the range), and (2) contribution of fine-mode aerosols to TOA reflectance is

418 small at the longer wavelengths ($\lambda > 1020$ nm) (thus change in refractive index has marginal

419 impact at the longer wavelengths). As a result, we assume the same imaginary part of the

420 refractive index throughout the VIIRS bands, and slightly reduced real part of the refractive

421 index for $\lambda > 1020$ nm, according to the water-soluble aerosol component at 70% relative

422 humidity introduced in *Hess et al.* [1998].

423   The extension for coarse-mode, however, should be handled carefully because both real

424 and imaginary parts of the refractive index vary within the AERONET wavelength range, and

425 are expected to change outside the range as well. In addition, it has strong effects on TOA

426 reflectance even at longer wavelengths due to the large particle size. It is well known that the

427 imaginary part of the refractive index of dust increases (SSA decreases) towards ultraviolet (UV)

428 wavelengths while showing small values (SSA generally higher than 0.95 based on AERONET

429 inversions) for $\lambda > \sim 600$ nm, as iron oxides in dust particles significantly absorb radiation in UV

430 through mid-visible wavelength range [*Gillespie and Lindberg*, 1992; *Sokolik and Toon*, 1999].

431 *Wagner et al.* [2012] suggest that the increase in the imaginary part of the refractive index with

432 decreasing wavelength can be characterized by a linear fit in both linear and logarithmic scale.

433 Accordingly, a linear interpolation/extrapolation in logarithmic scale is assumed for the

434 imaginary part of the refractive index while restraining the values higher than 0.0005 to keep the

435 value within the range that the single-scattering property database can handle. For real part, a

436 linear interpolation within 440 – 1020 nm and slightly reduced values for $\lambda > 1020$ nm are used

437 according to the spectral shape of feldspar particles [*Egan and Hilgeman*, 1979; *Smith and*

438 *Grainger*, 2014], which is the most abundant mineral group on Earth and is used as validation
439 target for the AERONET inversion algorithm.

440 Finally, the real and imaginary parts of the refractive index are increased and decreased
441 by 5% and 40%, respectively. Final values used in SOAR are shown in Table 3. These
442 adjustments are semi-empirical and improve the agreement with independent AERONET direct-
443 Sun AOD/AE data. The real parts of the refractive indices remain in-family, while the imaginary
444 counterparts decrease somewhat; however, the magnitudes are reasonable as they are smaller
445 than the level of uncertainties in AERONET refractive index [*Dubovik et al.*, 2000, 2006], i.e.
446 ±0.04 and ±50% for real and imaginary parts respectively. While empirical adjustments are best
447 avoided where possible, the AERONET inversions have some limitations which can lead to
448 suboptimal performance when results are applied to different studies. Of particular relevance to
449 the present study are that:

450 1. The current version 2 inversions use a scalar radiative transfer code (rather than a
451 vector code like VLIDORT). Scalar codes lead to biases in simulations of absorbing aerosols,
452 such as dust [e.g. *Levy et al.*, 2004]. A future AERONET version 3 will use a vector code [S.
453 Korkin/A. Sinyuk, personal communication, 2017], which should remove this error source.

454 2. The spheroidal aspect ratio distribution used by the AERONET team is itself empirical,
455 as it was optimized to match observations of real dust (which is neither spherical nor truly
456 spheroidal) phase functions in the midvisible spectral region [*Dubovik et al.*, 2006]. The resulting
457 particle shape distribution, which is also adopted in the current study, may therefore be less
458 appropriate for simulations of dust at longer wavelengths. In this regard, adjusting the assumed
459 refractive indices at these wavelengths can ameliorate these errors.

460 3. As noted earlier, AERONET assumes particles of all sizes to have the same refractive
461 index, even though they may be of chemically distinct origins. In the present study the influence
462 of this assumption was reduced by filtering AERONET inversions based on FMF to isolate dust-
463 dominated scenes, although it could still be a factor.

464 Thus, while the AERONET inversions provide an excellent baseline from which to start,
465 it is reasonable to make adjustments within this magnitude to improve the agreement with
466 validation data (the AERONET direct-Sun data being independent of the AERONET inversions).
467 It is hoped that revisiting the analysis with a future AERONET version may reduce or remove
468 the extent to which empirical adjustments are necessary.

469

Table 3. Complex refractive index of fine- and coarse-mode dust optical models for VIIRS bands, used in SOAR version 1.

Size mode	Refractive index for SOAR bands (n+ik)						
	488 nm	555 nm	672 nm	865 nm	1240 nm	1610 nm	2250 nm
Fine	1.43+0.001i	1.43+0.001i	1.43+0.001i	1.43+0.001i	1.41+0.001i	1.40+0.001i	1.38+0.001i
Coarse	1.54+0.0016i	1.54+0.0012i	1.54+0.0007i	1.52+0.0006i	1.49+0.0005i	1.48+0.0005i	1.47+0.0005i

472

4 Effects of New Dust Optical Model on SOAR Aerosol Product

4.1 Validation against AERONET

VIIRS SOAR retrievals are evaluated at Capo Verde, Gosan (South Korea), KAUST Campus (Saudi Arabia), Karachi (Pakistan), and Lampedusa (Italy) AERONET sites where dust events are observed to greater or lesser extents. To this end, a spherical dust optical model (and lookup table) is also created using the same microphysical and optical properties as the spheroidal counterpart except for the particle shape. The SOAR retrievals between spheroidal and spherical dust optical models are then compared to examine the effects of the new optical models on the retrieval performance. We only consider the quality-assured Level 2 aerosol product (quality flag = 3) for VIIRS, and the VIIRS data within 25 km of AERONET sites and AERONET data within ±30 min of VIIRS overpass time are averaged and compared. AERONET AOD is interpolated to 550 nm using the spectrally-closest wavelength and AERONET AE, which introduces negligible additional uncertainty. This has been the standard validation protocol for SOAR and many other satellite aerosol data products [e.g. *Sayer et al.,* 2012b, and references therein]. Note that the full SOAR algorithm is run, in which the retrieval selects the best-fitting aerosol optical model and there is no regional tuning. Thus, the retrieval is not forced to choose the dust model for these comparisons.

Tables 4 and 5 summarize the comparison statistics of AOD at 550 nm and AE, respectively, at the five locations. There are unfortunately only a limited number of AERONET coastal/island sites in dust-dominated areas available in the S-NPP era; those chosen cover several different dust aerosol source/transport regions. A forthcoming companion paper which describes the implementation of SOAR to VIIRS will include more validation results against global ship-based AOD measurements, including some dust areas. The comparison results reveal

better performance of the spheroidal optical model than the spherical counterpart for these sites. Depending on site, for AOD (AE), the Pearson coefficient increases from 0.76 – 0.93 (-0.02 – 0.71) for spherical model to 0.90 – 0.98 (0.52 – 0.80) for spheroidal model, the root-mean-square error (RMSE) decreases from 0.05 – 0.16 (0.34 – 0.50) to 0.04 – 0.13 (0.21 – 0.39), and the fraction within the expected error (EE, $\pm$0.03$\pm$10% for AOD) increases from 42% – 80% to 49% – 83%. Note that the EE refers to a confidence interval in which one standard deviation (~68%) of points are expected to lie with respect to a ground truth. This concept is the same as in other applications of SOAR and Deep Blue, and its values come from a combination of retrieval simulations and experience with similar algorithms and sensors [e.g. *Sayer et al.*, 2012a,b, 2013, 2014, 2015, 2017]. Thus, the target value overall for agreement within EE is ~68%; significantly more indicates retrieval errors are significantly smaller than expected, and vice versa.

For AOD, the median bias (MB) does not show significant differences between the two models likely due to cancelation of positive and negative biases when averaging. This implies that climatological AOD from the spherical model might not be significantly different from those of spheroidal model, although it is not immediately clear how long a data record must be aggregated to acquire unbiased results for the spherical model. Note that the smaller improvements at Gosan, Lampedusa, and Karachi than Capo Verde and KAUST Campus are associated with the smaller number of dust events for the former two sites, and local aerosol sources for Karachi (it is located in farther inland, and in a city of over 9 million people). The spheroidal model still slightly improves data quality at these locations where dust is less frequent (Gosan and Lampedusa); this also implies that the new dust model does not lead to a decreased performance for non-dust cases, for instance by choosing wrong aerosol model in the retrieval process.

Table 4. Comparison statistics of AOD between AERONET and VIIRS SOAR for spherical and spheroidal (in parentheses) dust models at Capo Verde, KAUST Campus, and Karachi. Statistics shown are the number of data points (N), Pearson coefficient (R), root-mean-squre error (RMSE), median bias (MB), and fraction within expected error (f). The expected error for AOD is defined as $\pm$(0.03+10%). Data from March 2012 to December 2016 are used.

Site name	Location (latitude, longitude, elevation)	N	R	RMSE	MB	f

Capo Verde	16.73°N, -22.93°E, 60 m	637	0.89	0.11	0.01	0.58
			(0.98)	(0.05)	(0.02)	(0.80)
Gosan	33.29°N, 126.16°E, 72 m	290	0.91	0.10	0.03	0.48
			(0.91)	(0.10)	(0.02)	(0.49)
KAUST	22.31°N, 39.10°E, 11 m	511	0.89	0.15	0.03	0.57
			(0.98)	(0.07)	(0.03)	(0.76)
Karachi	24.87°N, 67.03°E, 49 m	374	0.76	0.16	0.01	0.42
			(0.90)	(0.13)	(-0.03)	(0.46)
Lampedusa	12.63°N, 35.52°E, 45 m	724	0.93	0.05	0.01	0.80
			(0.95)	(0.04)	(0.01)	(0.83)

525

526 Table 5. Same as Table 4 except for the case of AE, and note there is no expected error defined
527 for AE.

Site name	Location	N	R	RMSE	MB
	(latitude, longitude, elevation)				
Capo Verde	16.73°N, -22.93°E, 60 m	637	-0.02	0.50	0.29
			(0.52)	(0.21)	(0.04)
Gosan	33.29°N, 126.16°E, 72 m	290	0.55	0.34	-0.04
			(0.59)	(0.32)	(-0.05)
KAUST	22.31°N, 39.10°E, 11 m	511	0.08	0.44	0.07
			(0.60)	(0.30)	(-0.11)
Karachi	24.87°N, 67.03°E, 49 m	374	0.48	0.37	0.07
			(0.80)	(0.24)	(-0.06)
Lampedusa	12.63°N, 35.52°E, 45 m	724	0.71	0.43	-0.21
			(0.80)	(0.39)	(-0.24)

528

529 Figure 5 shows scatterplots of AOD and AE at Capo Verde for which the current dust
530 optical model was created (thus, potentially showing the best results). Because other sites show
531 similar patterns, the same conclusions can be applied to them as well. First of all, we see that the
532 small difference in AOD MB between spherical and spheroidal models is indeed due to
533 cancelation of positive and negative errors when averaging. The scatterplot for spherical model
534 demonstrates larger scatter, with weak overestimation of a larger number of data points and
535 strong underestimation of a smaller number of data points, which resulted in a small positive MB
536 of 0.02. Next, it seems that the spherical dust model works reasonably well for AOD of 0 to
537 about 0.25 or 0.30, because in this AOD regime dust is likely mixed with spherical marine and/or

538   other background aerosol types. Finally, the impact of using the spheroidal dust optical model is

539   significant for AE, which implies that inaccurate FMF retrievals (as well as unrealistic phase

540   function) from using the spherical assumption can exacerbate the biases in spectral AOD. This is

541   consistent with other studies [e.g. *Levy et al.* 2003; *Remer et al.*, 2005; *Banks et al.* 2016].

542
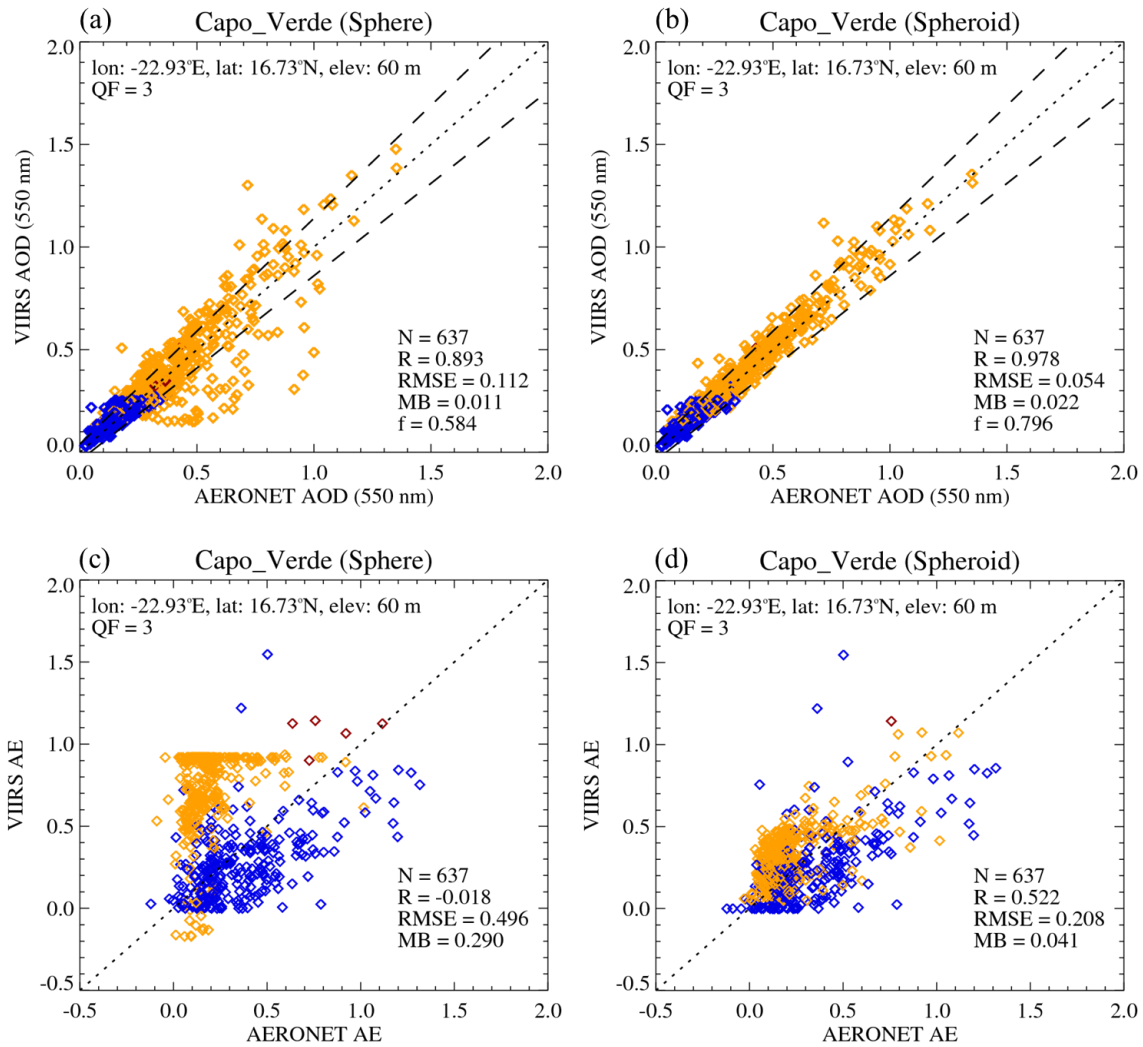
543

544   Figure 5. Scatter plots of (a, b) AOD at 550 nm and (c, d) AE between AERONET and VIIRS

545   SOAR at Capo Verde from March 2012 to December 2016. SOAR results are shown assuming

546   (a, c) spherical and (b, d) spheroidal dust optical models. Colors represent the best-fit aerosol

547   optical model determined by SOAR for each case; dust is in yellow, marine in blue, and fine-

548   dominated (rare for this site) in red. For AOD comparisons, dashed lines show the expected error

549   interval.

550

To further examine the effects of the spheroidal dust optical models, Figure 6 illustrates the retrieval errors as a function of scattering angle and AE (as a proxy of dust fraction, i.e., lower AE corresponds to higher dust fraction). We find that the spheroidal optical model effectively mitigates the well-known scattering angle dependence of AOD (positive bias in the side-scattering direction and low negative in the backscattering direction) of the spherical assumption. The spheroidal model results in a slight positive bias regardless of scattering angle, which is likely related to the slight positive bias in AE (Figure 5d). Although the bias can be further improved by adjusting the mode radius and/or refractive index of the coarse-mode dust optical model, additional adjustment is not made as the single optical model is used for dust over the global water surfaces in this version of the algorithm.

561
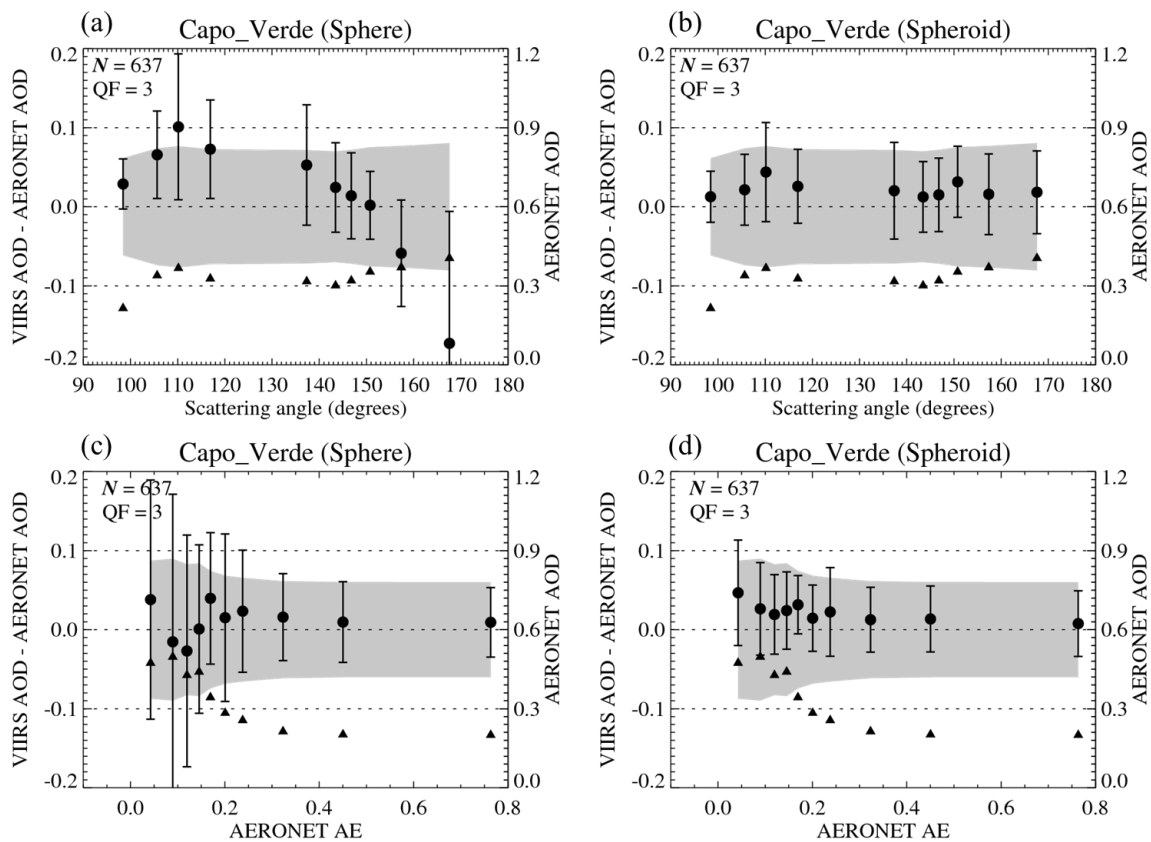
Figure 6. Mean and standard deviation of AOD errors in SOAR retrievals at Capo Verde site as a function of (a, b) scattering angle and (c, d) AE for (a, c) spherical and (b, d) spheroidal dust optical models. Data in 10 equal-number-of-data bins are shown with mean AERONET AOD in

566 triangle (corresponding to the right y-axis). Shaded area is the expected error envelope for the
567 mean AOD.

568

569   The results as a function of AE reveal that the spherical model leads to a larger AOD
570 scatter in lower AE regime (AE < 0.3) due to an inaccurate representation of dust phase function
571 (and particle size), which is significantly improved in the case of the spheroidal model. The
572 increasing positive bias with decreasing AE for the spheroidal model case implies a limitation of
573 the fixed size distribution and refractive index of the dust optical model. As it is not clear how
574 accurately the changing microphysical and optical properties can be modeled as a function of
575 various parameters (AOD, transport distance, etc.), further investigations are underway.

576

577 4.2 Spatial distribution

578   The scattering angle dependence of AOD resulting from the spherical assumption creates
579 an artificial spatial pattern in AOD maps, since the scattering angle changes significantly with
580 the satellite viewing geometry. For satellite sensors in Sun-synchronous orbits such as VIIRS,
581 the scattering angle, thus AOD bias, depends heavily on the cross-track scan angle, causing a
582 characteristic east-west pattern of AOD. At low to mid-latitudes the largest scattering angle
583 occurs near the sub-satellite point, slightly shifted toward east side of the scan for VIIRS, and it
584 decreases with increasing scan angle in both directions. Therefore, AOD retrieved using a
585 spherical dust optical model can show an artificial wave-like pattern due to the scattering angle
586 change.

587   Figure 7 shows an example of the artificial spatial pattern for a dust event observed on 17
588 July 2012, which is significantly lessened with the use of the spheroidal optical model. As
589 inferred from the scattering angle dependence of AOD, the spherical assumption leads to a
590 significant underestimation of AOD (as high as 0.5 or 50%) in the eastern part of the Sun glint
591 region, which occurs near the sub-satellite point shifted toward west, and a less significant
592 overestimation (~0.1 or 20%) in the western part of Sun glint due to smaller difference in the
593 phase function between the spherical and spheroidal dust optical models (Figure 7c). This creates
594 a sudden dip and jump in AOD before and after crossing the sun glint region, causing an
595 unnatural wave pattern in AOD. As inferred from Panels b and d in Figure 7, the spheroidal
596 model creates a more natural AOD gradient along the transport path of the Saharan dust (AOD

597 decreasing with transport distance), which has implications for satellite-based dust transport
598 studies [e.g. *Yu et al.*, 2013].

599
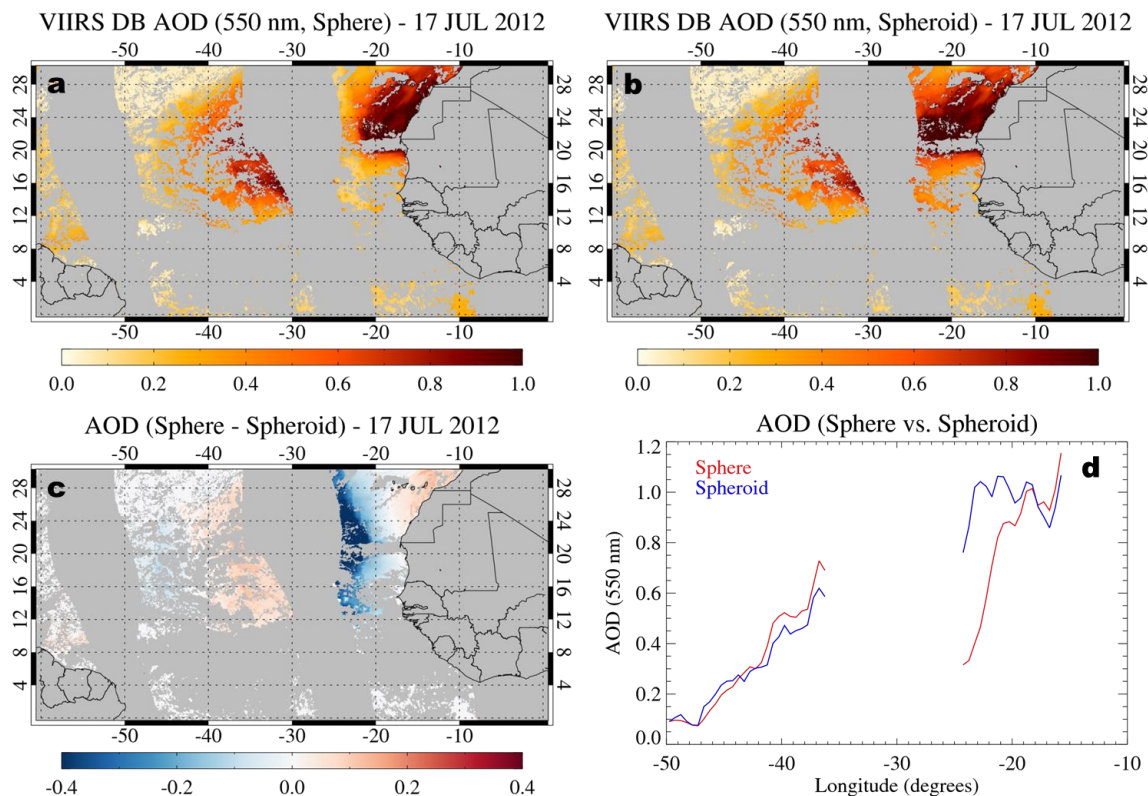
600
601 Figure 7. SOAR AOD map using (a) spherical and (b) spheroidal dust optical models for a
602 Saharan dust event on 17 July 2012, (c) AOD difference (spherical − spheroidal), and (d) AOD
603 longitudinal cross section from -50°E ~ -15°E at 23.75°N, for data gridded at 0.5° resolution.

604

605   While Figure 7 shows angular artifacts from the spherical assumption on an instantaneous
606 basis, it is relevant to consider whether such artifacts persist in temporally-aggregated data.
607 Monthly mean AOD shown in Figure 8 suggests that the spherical model leads to nonnegligible
608 biases up to 25% as compared to the spheroidal model, although the absolute error is much
609 smaller than the instantaneous case. In this specific case, the biases seem to exacerbate the
610 inherent wave pattern in AOD, as the spherical assumption tends to overestimate (underestimates)
611 AOD over regions with high (low) AOD. This implies that monthly means, which are frequently
612 used for various scientific applications, might not be sufficient for these biases from spherical
613 assumption to cancel out. In addition, it is not clear to what extent aggregations over longer

periods of time will improve the bias. It should be noted that the spheroidal model does not fully eliminate the wave pattern, which arises as a result of sampling due to the interaction between the orbital characteristics of S-NPP (and other polar-orbiting platforms) and timescales of dust transport and synoptic scale weather patterns.
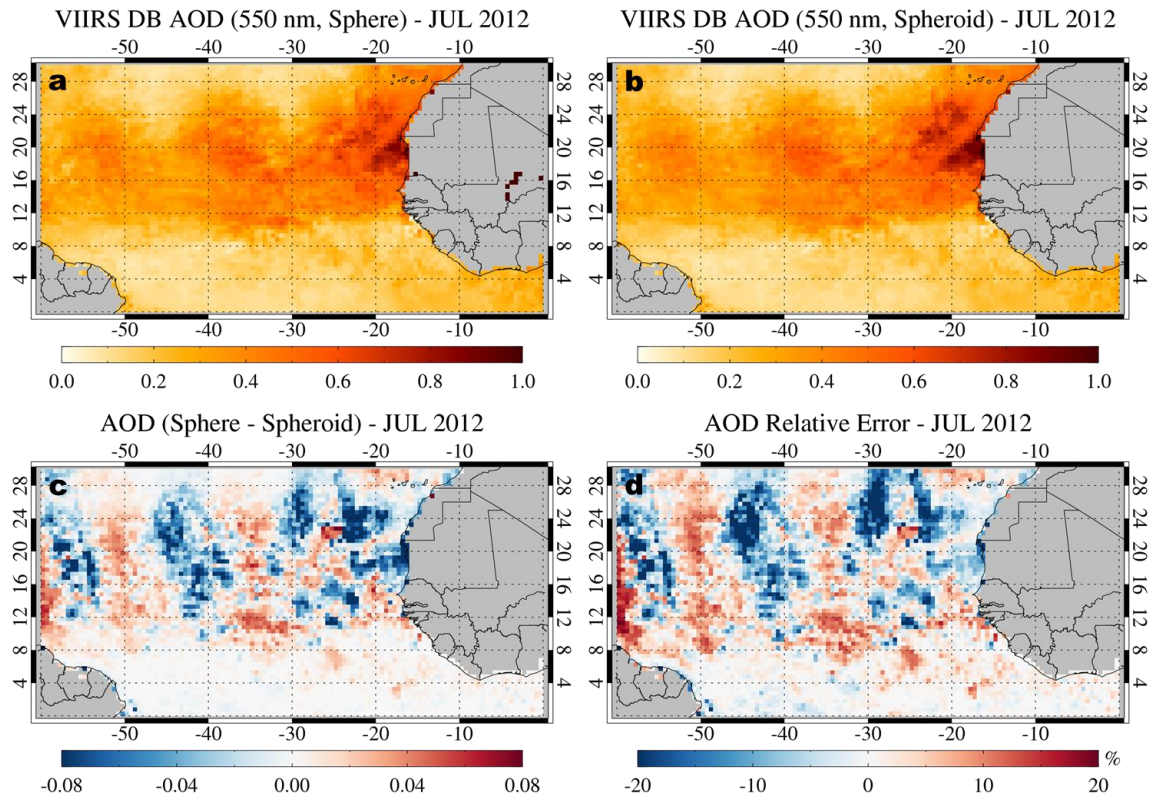
Figure 8. Monthly mean SOAR AOD maps from (a) spherical and (b) spheroidal dust optical models over the Atlantic Ocean in July 2012, and the (c) absolute and (d) relative AOD error of the spherical model as compared to the spheroidal model. The relative error is shown in percentage. Data gridded at 0.5° resolution are shown.

5 Summary and Conclusions

We presented a methodology for developing nonspherical dust optical models based on AERONET inversion data for use in the SOAR algorithm that will create the Version 1 VIIRS Deep Blue aerosol data product, which is planned to be released to the public in late 2017. These models can be used for other aerosol remote sensing or modeling purposes as well. We account for nonsphericity of dust particles by incorporating the same spheroid shape distribution as used

631 in the AERONET inversion algorithm when integrating the optical properties of the single
632 particle database used in this development. By doing so, the consistency between the aerosol
633 optical models and sky radiances observed by AERONET could be preserved.

634   Considering the significant contribution of Saharan dust over the global ocean, we use the
635 coarse-mode dust optical model optimized for the Capo Verde site combined with the weakly
636 absorbing fine-mode model, for the initial data processing. It was found that the dust optical
637 model, although optimized for a specific site, is representative for dust from various source
638 regions, showing intermediate properties of them. Preliminary validation against AERONET
639 direct-Sun observations (independent from the inversions used to develop the optical model)
640 suggested that the new dust optical model effectively mitigates the artificial scattering angle
641 dependence of AOD (and AE) found when spherical dust is assumed, resulting in significant
642 improvements in comparison statistics except for median bias. The similar median bias between
643 spherical and spheroidal models implied that climatological data from spherical assumption
644 might be as useful as those from more advanced spheroidal assumption. However, it was
645 revealed that there was still noticeable difference between the two in monthly mean data sets.
646 Although averaging for a longer-term period might reduce the difference further, it also limits
647 applications due to the averaging of the temporal signature of dust storms. Thus, the spheroidal
648 assumption is superior in a climatological sense as well. In addition to AOD, the spheroidal
649 model reduces the bias in AE (or FMF), which has implications for scientific applications where
650 aerosol size information is of importance.

651   The scattering angle dependence of AOD also caused an artificial spatial pattern, which
652 was improved when considering spheroidal model, in daily and monthly AOD maps. The
653 improvement is expected to contribute to more accurate quantification of dust transport with the
654 VIIRS' broad (3,040 km) swaths.

655   Since present approach is limited by the availability of AERONET inversion data, it is
656 not trivial to create optical models for the dust sources that are not well-sampled by AERONET
657 (e.g. Namib/Kalahari deserts, central Australia, Patagonia, Alaska). Thus, future attention to
658 these regions is desired to achieve more complete set of dust optical models over the globe.

659   Although this study only focused on implementing the dust optical models in the VIIRS
660 SOAR algorithm, ongoing development of the Deep Blue land algorithm also shows promising
661 results when incorporating similar optical models. More tests are underway to find an optimal

662   utilization of the new optical models in the land algorithm. With the inclusion of data over water

663   surfaces, improved performance, and wider swath than MODIS, the VIIRS Deep Blue product

664   suite will provide an enhanced view of global aerosol properties.

665

674

References

Ångström, A. (1929), On the atmospheric transmission of Sun radiation and on dust in the air, *Geogr. Ann., 11*, 156-166.

Alam, K., T. Trautmann, and T. Blaschke (2011), Aerosol optical properties and radiative forcing over mega-city Karachi, *Atmos. Res., 101*, 773-782, doi:10.1016/j.atmosres.2011.05.007.

Banks, J. R., H. E. Brindley, G. Stenchikov, and K. Schepanski (2016), Satellite retrievals of dust aerosol over the Red Sea, 2005–2015, *Atmos. Chem. Phys. Discuss.*, doi:10.5194/acp-2016-871.

Bohren, C. F., and D. R. Huffman (1983), *Absorption and Scattering of Light by Small Particles*, Wiley, New York.

Bi, L., P. Yang, G. W. Kattawar, and R. Kahn (2009), Single-scattering properties of triaxial ellipsoidal particles for a size parameter range from the Rayleigh to geometric-optics regimes, *Appl. Opt., 48*, 114-126, doi:10.1364/AO.48.000114.

Buchard, V., A. M. da Silva, P. R. Colarco, A. Darmenov, C. A. Randles, R. Govindaraju, O. Torres, J. Campbell, and R. Spurr (2015), Using the OMI aerosol index and absorption aerosol optical depth to evaluate the NASA MERRA Aerosol Reanalysis, *Atmos. Chem. Phys., 15*, 5743-5760, doi:10.5194/acp-15-5743-2015.

Chin, M., et al. (2014), Multi-decadal aerosol variations from 1980 to 2009: a perspective from observations and a global model, *Atmos. Chem. Phys., 14*, 3657-3690, doi:10.5194/acp-14-3657-2014.

Colarco, P. R., R. A. Kahn, L. A. Remer, and R. C. Levy (2014), Impact of satellite viewing-swath width on global and regional aerosol optical thickness statistics and trends, *Atmos. Meas. Tech., 7*, 2313-2335, doi:10.5194/amt-7-2313-2014.

Cziczo, D. J., K. D. Froyd, C. Hoose, E. J. Jensen, M. Diao, M. A. Zondlo, J. B. Smith, C. H. Twohy, and D. M. Murphy (2013), Clarifying the Dominant Sources and Mechanisms of Cirrus Cloud Formation, *Science, 340*, 1320-1324, doi:10.1126/science.1234145.

Draine, B. T., and P. J. Flatau (1994), Discrete-dipole approximation for scattering calculations, *J. Opt. Soc. Am. A, 11*, 1491-1499, doi:10.1364/JOSAA.11.001491.

Dubovik, O., and M. D. King (2000), A flexible inversion algorithm for retrieval of aerosol optical properties from Sun and sky radiance measurements, *J. Goephys. Res., 105*, 20673-20696, doi:10.1029/2000JD900282.

Dubovik, O., A. Smirnov, B. N. Holben, M. D. King, Y. J. Kaufman, T. F. Eck, and I. Slutsker (2000), Accuracy assessments of aerosol optical properties retrieved from Aerosol Robotic Network (AERONET) Sun and sky radiance measurements, *J. Geophys. Res., 105*, 9791-9806, doi:10.1029/2000JD900040.

Dubovik, O., B. Holben, T. F. Eck, A. Smirnov, Y. J. Kaufman, M. D. King, D. Tanre, and I. Slutsker (2002), Variability of absorption and optical properties of key aerosol types observed in worldwide locations, *J. Atmos. Sci., 59*, 590-608, doi:10.1175/1520-0469(2002)059<0590:VOAAOP>2.0.CO;2.

Dubovik, O., et al. (2006), Application of spheroid models to account for aerosol particle nonsphericity in remote sensing of desert dust, *J. Geophys. Res., 111*, D11208, doi:10.1029/2005JD006619.

Eck, T. F., B. N. Holben, J. S. Reid, O. Dubovik, A. Smirnov, N. T. O'Neill, I. Slutsker, and S. Kinne (1999), Wavelength dependence of the optical depth of biomass burning, urban, and desert dust aerosols, *J. Geophys. Res., 104*, 31333-31349, doi:10.1029/1999JD900923.

Eck, T. F., et al. (2008), Spatial and temporal variability of column-integrated aerosol optical properties in the southern Arabian Gulf and United Arab Emirates in summer, *J. Geophys. Res., 113*, D01204, doi:10.1029/2007JD008944.

Eck, T. F., et al. (2010), Climatological aspects of the optical properties of fine/coarse mode aerosol mixtures, *J. Geophys. Res., 115*, D19205, doi:10.1029/2010JD014002.

Egan, W. G. and T. W. Hilgeman (1979), *Optical properties of inhomogeneous materials: applications to geology astronomy chemistry and engineering*, Academic Press, NewYork.

Feng, Q., P. Yang, G. W. Kattawar, C. N. Hsu, S.-C. Tsay, and I. Laszlo (2009), Effects of particle nonsphericity and radiation polarization on retrieving dust properties from MODIS observations, *J. Aerosol Sci., 40*, 776-789, doi:10.1016/j.jaerosci.2009.05.001.

Gillespie, J. B. and J. D. Lindberg (1992), Ultraviolet and visible imaginary refractive index of strongly absorbing atmospheric particulate matter, *Appl. Opt., 31*, 2112-2115.

Giorgi, F. (1986), A particle dry-deposition parameterization scheme for use in tracer transport models, *J. Geophys. Res., 91*, 9794-9806, doi:10.1029/JD091iD09p09794.

Hansen, J. E., and L. D. Travis (1974), Light scattering in planetary atmospheres. *Space Sci. Rev.* 16, 527–610.

Hess, M., P. Koepke, and I. Schult (1998), Optical properties of aerosols and clouds: The software package OPAC, *Bull. Am. Met. Soc., 79*, 831-944, doi:10.1175/1520-0477(1998)079.

Holben, B. N., et al. (1998), AERONET−A federated instrument network and data archive for aerosol characterization, *Remote Sens. Environ., 66*, 1-16, doi:10.1016/S0034-4257(98)00031-5.

Holben, B. N., T. F. Eck, I. Slustker, A. Smirnov, A. Sinyuk, J. Shafer, D. Giles, and O. Dubovik (2006), AERONET's version 2.0 quality assurance criteria, *Proc. SPIE, 6408*, 64080Q, doi: 10.1117/12.706524.

Hsu, N. C., S.-C. Tsay, M. D. King, and J. R. Herman (2004), Aerosol properties over bright-reflecting source regions, *IEEE Trans. Geosci. Remote Sens., 42*, 557-569, doi:10.1109/TGRS.2004.824067.

Hsu, N. C., S.-C. Tsay, M. D. King, and J. R. Herman (2006), Deep blue retrievals of Asian aerosol properties during ACE-Asia, *IEEE Trans. Geosci. Remote Sens., 44*, 3180-3195, doi:10.1109/TGRS.2006.879540.

Hsu, N. C., M.-J. Jeong, C. Bettenhausen, A. M. Sayer, R. Hansell, C. S. Seftor, J. Huang, and S.-C. Tsay (2013), Enhanced Deep Blue aerosol retrieval algorithm: The second generation, *J. Geophys. Res. Atmos., 118*, 9296-9315, doi:10.1002/jgrd.50712.

Kahn, R., R. West, D. McDonald, B. Rheingans, and M. I. Mishchenko (1997), Sensitivity of multiangle remote sensing observations to aerosol sphericity, *J. Geophys. Res., 102*, 16861-16870, doi:10.1029/96JD01934.

Kaufman, Y. J., D. Tanré, and O. Boucher (2002), A satellite view of aerosols in the climate system, *Nature, 419*, 215-223, doi:10.1038/nature01091.

Kemppinen, O., T. Nousiainen, S. Merikallio, and P. Räisänen (2015), Retrieving microphysical properties of dust-like particles using ellipsoids: the case of refractive index, *Atmos. Chem. Phys., 15*, 11117-11132, doi:10.5194/acp-15-11117-2015.

Kok, J. F. (2011), Does the size distribution of mineral dust aerosols depend on the wind speed at emission?, *Atmos. Chem. Phys., 11*, 10149-10156, doi:10.5194/acp-11-10149-2011.

Lee, J., J. Kim, P. Yang, and N. C. Hsu (2012), Improvement of aerosol optical depth retrieval from MODIS spectral reflectance over the global ocean using new aerosol models archived from AERONET inversion data and tri-axial ellipsoidal dust database, *Atmos. Chem. Phys., 12*, 7087-7102, doi:10.5194/acp-12-7087-2012.

Lee, J., J. Kim, and Y. G. Lee (2014), Simultaneous retrieval of aerosol properties and clear-sky direct radiative effect over the global ocean from MODIS, *Atmos. Environ., 92*, 309-317, doi:10.1016/j.atmosenv.2014.04.021.

Levy, R. C., L. A. Remer, D. Tanré, Y. J. Kaufman, C. Ichoku, B. N. Holben, J. M. Livingston, P. B. Russell, and H. Maring (2003), Evaluation of the Moderate-Resolution Imaging Spectroradiometer (MODIS) retrievals of dust aerosol over the ocean during PRIDE, *J. Geophys. Res., 108*, doi:10.1029/2002JD002460.

Levy, R. C., L. A. Remer, Y. J. Kaufman (2004), Effects of neglecting polarization on the MODIS aerosol retrieval over land, *IEEE Trans. Geosci. Remote Sens., 42*(11), 2576-2583, doi;10.1109/TGRS.2004.837336.

Li, F., A. M. Vogelmann, and V. Ramanathan (2004), Saharan dust aerosol radiative forcing measured from space, *J. Clim., 17*, 2558-2571, doi:10.1175/1520-0442(2004)017<2558:SDARFM>2.0.CO;2.

Liao, H., and J. H. Seinfeld (1998), Radiative forcing by mineral dust aerosols: sensitivity to key variables, *J. Geophys. Res., 103*, 31637-31645, doi:10.1029/1998JD200036.

Lin, J. J., K. E. Noll, and T. M. Holsen (1994), Dry deposition velocities as a function of particle-size in the ambient atmosphere, *Aerosol Sci. Tech., 20*, 239-252, doi:10.1080/02786829408959680.

Masuda, K., Y. Mano, H. Ishimoto, M. Tokuno, Y. Yoshizaki, and N. Okawara (2002), Assessment of the nonsphericity of mineral dust from geostationary satellite measurements, *Remote Sens. Environ., 82*, 238-247, doi:10.1016/S0034-4257(02)00040-8.

Meng, Z., P. Yang, G. W. Kattawar, L. Bi, K. N. Liou, and I. Laszlo (2010), Single-scattering properties of tri-axial ellipsoidal mineral dust aerosols: A database for application to radiative transfer calculations, *J. Aerosol Sci., 41*, 501-512, doi:10.1016/j.jaerosci.2010.02.008.

Mishchenko, M. I., I. V. Geogdzhayev, L. Liu, J. A. Ogren, A. A. Lacis, W. B. Rossow, J. W. Hovenier, H. Volten, and O. Muñoz (2003), Aerosol retrievals from AVHRR radiances:

effects of particle nonsphericity and absorption and an updated long-term global climatology of aerosol properties, *J. Quant. Spectrosc Ra., 75-80*, 953-972, doi:10.1016/S0022-4073(02)00331-X.

Mishchenko, M. I., and L. D. Travis (1994), T-matrix computations of light-scattering by large spheroidal particles, *Opt. Commun., 109*, 16-21, doi:10.1016/0030-4018(94)90731-5.

Mishchenko, M. I., L. D. Travis, R. A. Kahn, and R. A. West (1997), Modeling phase functions for dustlike tropospheric aerosols using a shape mixture of randomly oriented polydisperse spheroids, *J. Geophys. Res., 102*, 16831-16847, doi:10.1029/96JD02110.

O'Neill, N. T., T. F. Eck, A. Smirnov, B. N. Holben, and S. Thulasiraman (2003), Spectral discrimination of coarse and fine mode optical depth, *J. Geophys. Res., 108*, doi:10.1029/2002JD002975.

Remer, L. A., Y. J. Kaufman, D. Tanré, S. Mattoo, D. A. Chu, J. V. Martins, R.-R. Li, C. Ichoku, R. C. Levy, R. G. Kleidman, T. F. Eck, E. Vermote, and B. N. Holben (2005), The MODIS aerosol algorithm, products and validation, *J. Atmos. Sci., 62*, 947–973, doi:10.1175/JAS3385.1.

Sayer, A. M., N. C. Hsu, C. Bettenhausen, M.-J. Jeong, B. N. Holben, and J. Zhang (2012a), Global and regional evaluation of over-land spectral aerosol optical depth retrievals from SeaWiFS, *Atmos. Meas. Tech., 5*, 1761–1778, doi:10.5194/amt-5-1761-2012.

Sayer, A. M., N. C. Hsu, C. Bettenhausen, Z. Ahmad, B. N. Holben, A. Smirnov, G. E. Thomas, and J. Zhang (2012b), SeaWiFS Ocean Aerosol Retrieval (SOAR): Algorithm, validation, and comparison with other data sets, *J. Geophys. Res., 117*, D03206, doi:10.1029/2011JD016599.

Sayer, A. M., N. C. Hsu, C. Bettenhausen, and M.-J. Jeong (2013), Validation and uncertainty estimates for MODIS Collection 6 "Deep Blue" aerosol data, *J. Geophys. Res. Atmos., 118*, 7864-7872, doi:10.1002/jgrd.50600.

Sayer, A. M., L. A. Munchak, N. C. Hsu, R. C. Levy, C. Bettenhausen, and M.-J. Jeong (2014), MODIS Collection 6 aerosol products: Comparison between Aqua's e-Deep Blue, Dark Target, and "merged" data sets, and usage recommendations, *J. Geophys. Res. Atmos., 119*, 13965-13989, doi:10.1002/2014JD022453.

Sayer, A. M., N. C. Hsu, C. Bettenhausen, M.-J. Jeong, and G. Meister (2015), Effect of MODIS Terra radiometric calibration improvements on Collection 6 Deep Blue aerosol products:

Validation and Terra/Aqua consistency, *J. Geophys. Res. Atmos., 120*, 12,157-12,174, doi:10.1002/2015JD023878.

Sayer, A. M., N. C. Hsu, C. Bettenhausen, R. E. Holz, J. Lee, G. Quinn, and P. Veglio (2017), Cross-calibration of S-NPP VIIRS moderate-resolution reflective solar bands against MODIS Aqua over dark water scenes, *Atmos. Meas. Tech., 10*, 1425-1444, doi:10.5194/amt-10-1425-2017.

Scarnato, B. V., S. China, K. Nielsen, and C. Mazzoleni (2015), Perturbations of the optical properties of mineral dust particles by mixing with black carbon: a numerical simulation study, *Atmos. Chem. Phys., 15*, 6913-6928, doi:10.5194/acp-15-6913-2015.

Schuster, G. L., O. Dubovik, and A. Arola (2016), Remote sensing of soot carbon − Part 1: Distinguishing different absorbing aerosol species, *Atmos. Chem. Phys., 16*, 1565–1585, doi:10.5194/acp-16-1565-2016.

Smirnov, A., B. N. Holben, T. F. Eck, O. Dubovik, and I. Slutsker (2000), Cloud-screening and quality control algorithms for the AERONET database, *Remote Sens. Environ., 73*, 337-349, doi:10.1016/S0034-4257(00)00109-7.

Smith, A. J. A. and Grainger R. G. (2014), Does variation in mineral composition alter the short-wave light scattering properties of desert dust aerosol?, *J. Quant. Spectrosc. Ra., 133*, 235-243, doi:10.1016/j.jqsrt.2013.08.005.

Sokolik, I. N. and O. B. Toon (1999), Incorporation of mineralogical composition into models of the radiative properties of mineral aerosol from UV to IR wavelengths, *J. Geophys. Res., 104*, 9423-9444.

Spurr, R. (2006), VLIDORT: A linearized pseudo-spherical vector discrete ordinate radiative transfer code for forward model and retrieval studies in multilayer multiple scattering media, *J. Quant. Spectrosc. Ra., 102*, 316-342, doi:10.1016/j.jqsrt.2006.05.005.

Sugimoto, N., T. Nishizawa, A. Shimizu, I. Matsui, and H. Kobayashi (2015), Detection of internally mixed Asian dust with air pollution aerosols using a polarization optical particle counter and a polarization-sensitive two-wavelength lidar, *J. Quant. Spectrosc. Ra., 150*, 107-113, doi:10.1016/j.jqsrt.2014.08.003.

Tegen, I., P. Hollrig, M. Chin, I. Fung, D. Jacob, and J. Penner (1997), Contribution of different aerosol species to the global aerosol extinction optical thickness: Estimates from model results, *J. Geophys. Res., 102*, 23895-23915, doi:10.1029/97JD01864.

Wagner, R., T. Ajtai, K. Kandler, K. Lieke, C. Linke, T. Müller, M. Schnaiter, and M. Vragel (2012), Complex refractive indices of Saharan dust samples at visible and near UV wavelengths: a laboratory study, *Atmos. Chem. Phys., 12*, 2491–2512, doi:10.5194/acp-12-2491-2012.

Waterman, P. C. (1971), Symmetry, unitarity, and geometry in electromagnetic scattering, *Phys. Rev. D, 3*, 825–839.

Wang, J., X. Liu, S. A. Christopher, J. S. Reid, E. Reid, and H. Maring (2003), The effects of non-sphericity on geostationary satellite retrievals of dust aerosols, *Geophys. Res. Lett., 30*, doi:10.1029/2003GL018697.

Yang, P., and K. N. Liou (1995), Light scattering by hexagonal ice crystals: comparison of finite-difference time domain and geometric optics models, *J. Opt. Soc. Am. A, 12*, 162-176, doi:10.1364/JOSAA.12.000162.

Yang, P., and K. Liou (1996), Finite-difference time domain method for light scattering by small ice crystals in three-dimensional space, *J. Opt. Soc. Am. A, 13*, 2072-2085, doi:10.1364/JOSAA.13.002072.

Yang, P., K. N. Liou, M. I. Mishchenko, and B.-C. Gao (2000), Efficient finite-difference time domain scheme for light scattering by dielectric particles: application to aerosols, *Appl. Opt.*, 39, 3727-3737.

Yang, P., Q. Feng, G. Hong, G. W. Kattawar, W. J. Wiscombe, M. I. Mishchenko, O. Dubovik, I. Laszlo, and I. N. Sokolik (2007), Modeling of the scattering and radiative properties of nonspherical dust-like aerosols, *J. Aerosol Sci., 38*, 995-1014, doi:10.1016/j.jaerosci.2007.07.001.

Yee, S. K. (1966), Numerical solution of initial boundary value problems involving Maxwell's equations in isotropic media, *IEEE Trans. Antennas Propag.,* 14, 302–307.

Yin, Y., S. Wurzler, Z. Levin, and T. G. Reisin (2002), Interactions of mineral dust particles and clouds: Effects on precipitation and cloud optical properties, *J. Geophys. Res., 107*, doi:10.1029/2001JD001544.

Yoshioka, M., N. M. Mahowald, A. J. Conley, W. D. Collins, D. W. Fillmore, C. S. Zender, and D. B. Coleman (2007), Impact of desert dust radiative forcing on Sahel precipitation:

888   Relative importance of dust compared to sea surface temperature variations, vegetation
889   changes, and greenhouse gas warming, *J. Clim., 20*, 1445-1467, doi:10.1175/JCLI4056.1.
890 Yu, H., L. A. Remer, R. A. Kahn, M. Chin, and Y. Zhang (2013), Satellite perspective of aerosol
891   intercontinental transport: From qualitative tracking to quantitative characterization, *Atmos.*
892   *Res., 124*, 73-100, doi: 10.1016/j.atmosres.2012.12.013
893 Yurkin, M. A., V. P. Maltsev, and A. G. Hoekstra (2007), The discrete dipole approximation for
894   simulation of light scattering by particles much larger than the wavelength, *J. Quant.*
895   *Spectrosc. Ra., 106*, 546-557, doi:10.1016/j.jqsrt.2007.01.033.